Corrosion Science 49 (2007) 920–938.
www.elsevier.com/locate/corsci
doi:10.1016/j.corsci.2006.05.037

Quantitative study of exfoliation corrosion: Exfoliation of slices in humidity technique

Xinyan Zhao, G.S. Frankel *

Fontana Corrosion Center, Department of Materials Science and Engineering, The Ohio State University.

Abstract

A new technique, exfoliation of slices in humidity (ESH), was developed for the determination of exfoliation corrosion (EFC) susceptibility and quantification of EFC kinetics. Two AA7178 plates taken from the wingskin of a retired KC135 airplane were used as test samples. Slices of the plate were pretreated by potentiostatic polarization in chloride solution to develop localized corrosion sites. Subsequent exposure to high humidity after pretreatment of properly oriented and unconstrained samples resulted in the development of EFC at the edges of the slices. The EFC kinetics were determined by measuring the width of the central unattacked region of the samples. The ESH results were representative of the different EFC behavior of the two plates during outdoor exposure. These results show the capability of the ESH test to discriminate between plates of varying susceptibility and to determine EFC rates quantitatively. The different susceptibility of the two plates to EFC was attributed to differences in microstructure and grain boundary chemistry.

1. Introduction

Exfoliation corrosion (EFC) is a particular form of intergranular corrosion that is often observed on the surface of wrought aluminum alloys with an elongated grain structure [1]. When intergranular corrosion proceeds along intergranular paths parallel to the surface, the hydrated aluminum oxide corrosion product has a higher volume than the alloy matrix from which the product formed. Consequently, relatively large wedging stresses are produced, which lift the surface grains, giving rise to a layered appearance. EFC is a significant source of life-limiting degradation in airframes [2]. It consumes load bearing cross section and increases the stress in the remaining intact material, resulting in a loss in mechanical properties of Al alloys.

The susceptibility of Al alloys to EFC can be assessed by exposure testing. ASTM G-34, known as the EXCO test, involves exposure to an oxidizing acidic chloride solution and comparison of the resulting surface to standard photographs [1,3]. Other tests involving exposure to aggressive environments have been devised, including the ASSET and MAST-MAASIS tests. In these methods, salt solutions are alternately sprayed onto the surface of the specimens and the resulting surfaces are evaluated to determine the EFC susceptibility [4–7]. The behavior of Al alloys in these accelerated environments has been correlated to long-term exposure in less-aggressive natural environments [8–10]. As a result, these tests are very useful for assessing susceptibility to EFC attack. However, they do not provide quantitative measurements of susceptibility or growth kinetics, which are required for predictive modeling of corrosion development. Liddiard and coworkers have used a deflection technique to quantify exfoliation extent and determine EFC kinetics [11]. In this technique, the effective remaining load-bearing section of specimens exhibiting EFC was determined from their compliance under four-point

bending. The rate of EFC can be assessed from periodic measurements. The deflection technique is valid only when the thinning of the specimen during corrosion is uniform.

The alloy grain shape is thought to be an important factor in exfoliation corrosion. Robinson et al. found that the severity of exfoliation corrosion is related to the grain aspect ratio of the material [12–14]. More elongated grain shape results in severe exfoliation corrosion. Besides elongated grain structure, grain boundary chemistry also plays an important role in the EFC susceptibility. It is well known that grain boundaries are often more susceptible to corrosion than the grain interiors because of the microstructural heterogeneity. The grain boundary region of a typical Al alloy can contain precipitates on the grain boundary and a precipitate free zone (PFZ) next to the grain boundary, which have very different electrochemical behavior than the grain interior region [15]. Maitra and English have attributed the IGC susceptibility of AA7075-T6 to Mg and Zn solute segregation or enrichment in the grain boundary region [16]. Ramgopal et al. proposed that IGC in 7075-T6 temper was caused by anodic dissolution of $Mg(ZnCuAl)_2$ [15,17]. Other investigations have suggested that the cause of exfoliation is an electrochemical potential developed between primary or secondary particles, which contain some or all of the elements Al, Fe, Si, Mn, Mg, and Zn, and the surrounding AlZnMg solid solution [18,19]. Evans proposed the possibility of an electrochemical cell occurring between Mn-rich and Mn-depleted regions. The Mn bearing particles precipitate preferentially in the center of the grains compared to the region near grain boundaries, resulting in differing electrochemical potential [5].

Determination of EFC kinetics is critical for the development of predictive failure models. The aim of this work was to develop a technique and analysis methodology that can provide quantitative measurement of exfoliation corrosion kinetics. The EFC rates of different AA7178 wingskin plates were determined and related to the alloy microstructure and compositions of the grain boundary constituents determined from analytical TEM techniques.

2. Experimental

2.1. Materials

Test samples were machined from a piece of a wingskin of a retired KC135 airplane. The wingskin section contained two AA7178-T6 plates attached to an underlying support beam by steel rivets. The wingskin section was divided into two parts. One part of the wingkin section was exposed in the uncoated condition at an atmospheric exposure test site near Daytona Beach, FL by W. Abbott of Battelle. The other part of the section was used to perform laboratory testing. Fig. 1 shows the section after 9 months exposure at Daytona Beach. The two plates in the section exhibited vastly different exfoliation behavior during the exposure near the seacoast. One of the plates exfoliated badly next to the steel rivets and the other plate only developed cosmetic surface attack. They are referred to as ‘‘good’’ and ‘‘bad’’ plates in reference to their EFC susceptibility. The compositions of the two plates were determined by Inductively Coupled Plasma Optical Emission Spectrometry, Table 1. The ‘‘good’’ plate had slightly lower levels of Zn, Cu, and Mg than the bad plates. However, both compositions were similar and within normal range for AA7178-T6, as were the hardness values [20].

Samples were machined from the ‘‘good’’ and ‘‘bad’’ plates in the shape of rectangular slices, as illustrated in Fig. 2. The slices were 3–4 cm long, and oriented such that the long axis of each slice was in the longitudinal orientation of the microstructure (along the rolling direction). The slice thickness, oriented in the plate transverse direction, was around 1 mm. The

width of each slice was the full plate through-thickness in the short transverse direction: 4.1 and 4.6 mm for the ‘‘good’’ and ‘‘bad’’ plates, respectively. The slice edges, which were the original outer surfaces of the plate, were lightly polished. All other faces were ground in ethanol to 800 grit finish, cleaned ultrasonically in ethanol, and finally dried by an air stream.

Detailed metallographic analysis was performed on T (long transverse), S (short transverse), and L (longitudinal) sections of the ‘‘good’’ and ‘‘bad’’ plates. Samples were

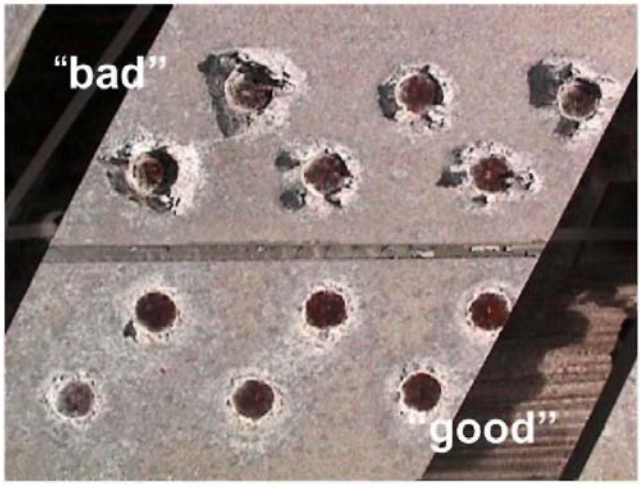

Fig. 1. Photo of AA7178 wingskin sample after 9 months of exposure at Daytona Beach. Sample was uncoated and had steel rivets attaching plates to understructure. Image provided by W. Abbott, Battelle.

Table 1
Composition of ‘‘good’’ and ‘‘bad’’ plates determined by ICP-OES.

	Al	Zn	Mg	Cu	Fe	Si	Mn	Cr	Ti
‘‘Good’’	Bal	7.03	2.62	2.06	0.25	0.05	0.03	0.21	0.04
‘‘Bad’’	Bal	7.25	2.81	2.17	0.18	0.04	0.01	0.21	0.02

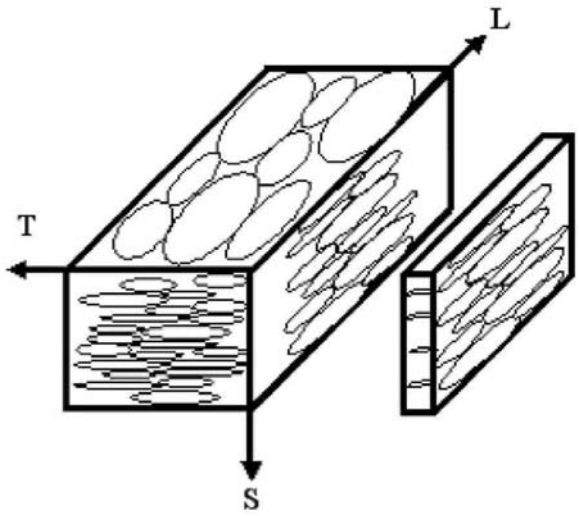

Fig. 2. Schematic drawing of orientation of slices for ESH test relative to elongated microstructure of AA7178 wingskin sample.

polished to 1 μm and chemically etched with Keller's reagent (2 ml HF, 3 ml HCl, 5 ml HNO_3 and 190 ml H_2O) to reveal the microstructure. Optical microscopy methods were used to examine metallographic sections in the three perpendicular orientations. The grain dimension in the three orientations as a function of the position along the through thickness direction was determined with the Clemex Vision image analysis software. The through thickness cross section was divided into 15 zones. In each zone, 30 grains were measured and the mean values were calculated to represent the grain size in each zone.

Analytical transmission electron microscopy (TEM) was performed to investigate the local chemistry at the grain boundaries. A 10 mm long sample was cut from a T section of the ''good'' plate. The width of the sample was the whole thickness of the plate. The sample surface was polished with 0.5 μm alumina suspended in ethanol and slightly etched with acid reagent (6 ml HF, 40 ml H_2SO_4, 360 ml H_2O) for 20 s to reveal the grain boundaries on the surface. Cross sectional TEM samples were prepared by an FEI Strata Dual Beam 235 M scanning electron microscope (SEM)/focused ion beam (FIB) tool using a 30 keV Ga ion beam and a 5 keV electron beam. The TEM samples were made such that they contained a grain boundary located 10–30 μm away from the surface. TEM samples were made close to the upside surface (corresponding to the surface that was exposed to the Daytona Beach environment) and close to the downside surface (corresponding to the surface that was not exposed to the Daytona Beach environment). Prior to sectioning, specific sites near the specimen edge were located and identified by SEM/EDS in the FIB and then covered by deposition of a 1.5 μm-thick Pt layer to protect the specimen surface during the FIB sectioning. The membrane had an area of 15 μm × 5 μm and was thinned in the FIB to a thickness of 100 nm for electron transparency. The membrane was plucked out of the bulk sample under an optical microscope using a sharp Pyrex needle of 1 μm in diameter and placed on a 200 mesh Au TEM grid with a formvar/carbon support film for TEM analysis. The TEM observation was made in the region of the membrane above a hole in the mesh grid. TEM characterization of the FIB sectioned membranes was conducted using an FEI Tecnai TF20 scanning transmission electron microscope (STEM) operating at 200 kV. The probe size was <2 nm and the step size was 5 nm.

Electrochemical polarization measurements were performed on samples ground to 1200 grit. The solution was 1 M NaCl deareated with Ar gas to decrease the corrosion potential and allow for clear observation of the breakdown potentials. Potentiodynamic scans were performed at a rate of 0.1 mV/s. A Pt counter electrode and saturated calomel reference electrode (SCE) were used. All potentials in this paper are referenced vs. SCE.

2.2. Exfoliation of slices in humidity (ESH) technique

Samples sliced from the plates as described above were given a potentiostatic electrochemical pretreatment in 1 M NaCl at a potential of −710 mV SCE for 7 h. This potential is above the second breakdown potential for this material in this environment, which is −725 mV SCE as will be shown below. The purpose of the pretreatment was to initiate localized corrosion attack and develop an aggressive environment in the corrosion sites. This environment presumably contained sodium chloride from the pretreatment solution and aluminum alloy corrosion product. XPS analysis of samples given similar treatment found the presence of Al, O,

and Cl [21]. Following the pretreatment, the sample was rinsed with DI water and placed in a humidity chamber, consisting of a sealed beaker containing a saturated salt solution at room temperature (22-25^{0}C). The samples were held in the air space above the solution and a graph paper was placed behind them to facilitate the determination of EFC extent. Different saturated salt solutions were used to create a range of constant humidity: sodium sulfate (Na_2SO_4), ammonium chloride (NH_4Cl), potassium iodide (KI), potassium carbonate ($K_2CO_3 \cdot 2H_2O$), and calcium chloride ($CaCl_2 \cdot 6H_2O$). The relative humidities above saturated solutions of these salts measured by an RH meter were similar to handbook values [22], as is reported in Table 2. Pretreated samples developed EFC upon subsequent exposure to high humidity. The EFC started at the outer edges, corresponding to the original plate surfaces, and moved inward. Images of the samples were recorded by digital photography through the glass walls of the humidity chamber. The contrast between the boundary of the outer exfoliated and inner unattacked regions was sufficient to allow tracking of the EFC kinetics by analysis of the photographs.

Table 2
Humidity associated with saturated salt solutions

Salt	Expected %RH 22]	Measured %RH at RT
Na_2SO_4	93 at 20 ^{0}C	96
NH_4Cl	79.3 at 20 ^{0}C	76.5
KI	56.2 at 100 ^{0}C	65.1
$K_2CO_3 \cdot 2H_2O$	43 at 24.5 ^{0}C	49–50
$CaCl_2 \cdot 6H_2O$	32.3 at 20 ^{0}C	30.1

The width change of the inner unattacked region of an ESH sample can be related to the material loss due to exfoliation corrosion. The photographs of the ESH samples were analyzed to measure the unattacked width as a function of time. One measurement of the unattacked width was made on each sample at a position 10 mm from the top of the sample. This value was subtracted from the original width at this position, d_0, to determine the depth of metal consumed by EFC: $\Delta d_i = d_0 - d_i$, where i = 1,2,....day. Since the exfoliation occurred at the two edge surfaces, one half of the width change $\frac{\Delta d_i}{2}$ represents the average EFC depth.

3. Results and discussion

3.1. Electrochemical and ESH characterization

Potentiodynamic polarization curves of the ‘‘good’’ and ‘‘bad’’ plates were obtained in deareated 1 M NaCl at a potential sweep rate of 0.1 mVs^{-1}, Fig. 3. Both plates exhibited two breakdown potentials as has been observed for AA7xxx alloys in the underaged and peak aged conditions [23]. The values of the breakdown potentials are similar for the two plates, so the difference in exfoliation susceptibility cannot be attributed to a difference in breakdown potentials. There was, however, a difference in the magnitude of both the transient peak above the first breakdown potential and the current flowing at higher potentials; both were smaller for the ‘‘good’’ plate. This reflects some differences in the microstructure.

Samples of the ‘‘good’’ and ‘‘bad’’ plates from the AA7178 wingskin section were ESH-tested by electrochemical pretreatment and then exposure to 96% RH. Fig. 4 shows images of the

samples over a period of time from 0 (as-pretreated) to 52 days of high humidity exposure. The samples are oriented such that the rolling direction is vertical and the plate thickness is horizontal, with the original plate surfaces on the left and right edges of the samples.

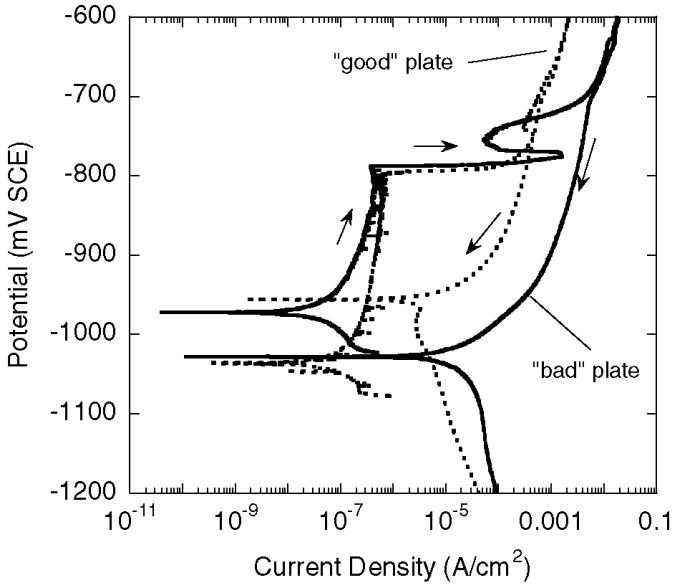

Fig. 3. Polarization curves of AA7178 ‘‘good’’ and ‘‘bad’’ sample in deareated 1.0 M NaCl at a scan rate of 0.1 mV/s.

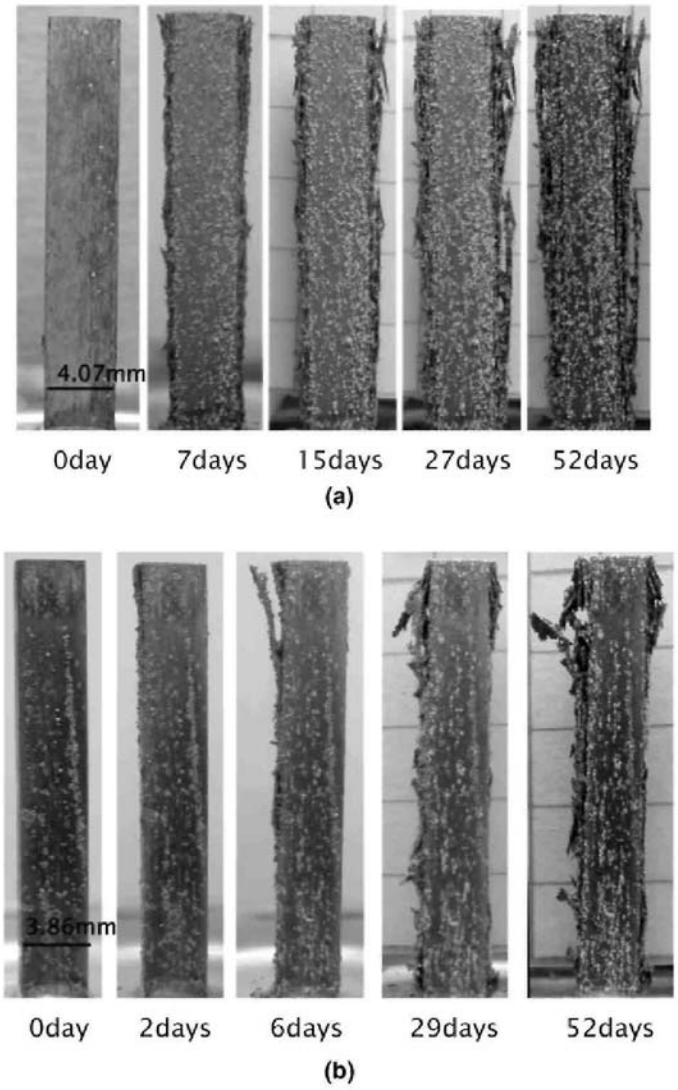

Fig. 4. Images of AA7178 wingskin samples exposed to 96% humidity following electrochemical pretreatment: (a) ‘‘bad’’ sample and (b) ‘‘good’’ sample.

After several days, EFC was evident on both edges of the slice from the ‘‘bad’’ plate and it continued to progress more or less evenly on both edges over the exposure period of almost 2 months, Fig. 4a. The behavior of the slice removed from the ‘‘good’’ plate behaved quite differently. One side of the sample (the left side of the images in Fig. 4b) exhibited severe EFC, while the other side of the sample was practically unattacked. The side of the slice that was not attacked in the ESH test corresponds to the side of the ‘‘good’’ plate that was exposed upwards to the environment at Daytona Beach. So the high resistance of the ‘‘good’’ plate to EFC was reproduced in the lab in that the surface exposed at Daytona Beach reacted slowly in the ESH test. This resistance was only representative of one surface; the other side of the ‘‘good’’ sample corresponding to the side of the plate that faced downward and was not exposed to the elements at Daytona Beach showed rapid attack in the ESH test. It is expected that the ‘‘good’’ plate would have exfoliated rapidly at Daytona Beach if the plate had been oriented such that the down

side had been facing upward. Overall, the ‘‘bad’’ sample was attacked much faster than the ‘‘good’’ sample.

As seen in Fig. 4, corrosion product exuded out of the surfaces (corresponding to the transverse face of the microstructure) of both good and bad samples upon exposure to 96% RH. This generation of corrosion product is evidence of continued corrosion at localized sites from the aggressive environment deposited in the microstructure during the electrochemical pretreatment. However, the EFC proceeded inward from the edges.

The kinetics of EFC can be determined by measuring the change in width of the central unexfoliated region. Fig. 5 shows the average exfoliation depth, which is equal to half of the change in width of the inner unexfoliated region. The ‘‘good’’ sample exfoliated primarily on one side, so the real EFC depth for the attacked side of the ‘‘good’’ sample is approximately twice the value given in Fig. 5. Considering this fact, the depth of EFC on the susceptible side of the ‘‘good’’ sample was approximately the same as the depth on both sides of the ‘‘bad’’ sample, which is evident in Fig. 4. Fig. 5 shows that the rate of EFC was not constant with time. For two samples, it started out rapidly, with a change of about 80 μm in the first day and then slowed to about 4 μm/day. The other two samples did not experience the initial rapid EFC and started off with a slow rate. It is interesting that the two ‘‘good’’ and two ‘‘bad’’ samples did not behave the same at the beginning. One of each type started out quickly and one started slowly. After about 2 weeks, the EFC rate for the ‘‘bad’’ samples and one of the ‘‘good’’ samples increased to a higher value, about 20 μm/day. The rate for each of these samples then decreased again to a lower value of about 2 μm/day. The other ‘‘good’’ sample (the one shown in Fig. 4b) did not exhibit an increase again until after 35 days. These results indicate that there are zones of the plate through the thickness with varying susceptibility and EFC kinetics. The apparent resistance of the ‘‘good’’ plate during outdoor exposure at Daytona Beach was caused by the seemingly chance location of a resistant zone at the upward-facing surface of that plate. It is interesting that zones of varying EFC susceptibility exist through the thickness of a plate.

This has never been reported, but other techniques, such as the EXCO tests, do not have the sensitivity to find these zones. This varying susceptibility could be caused by variations in microstructure or residual stress in the plate.

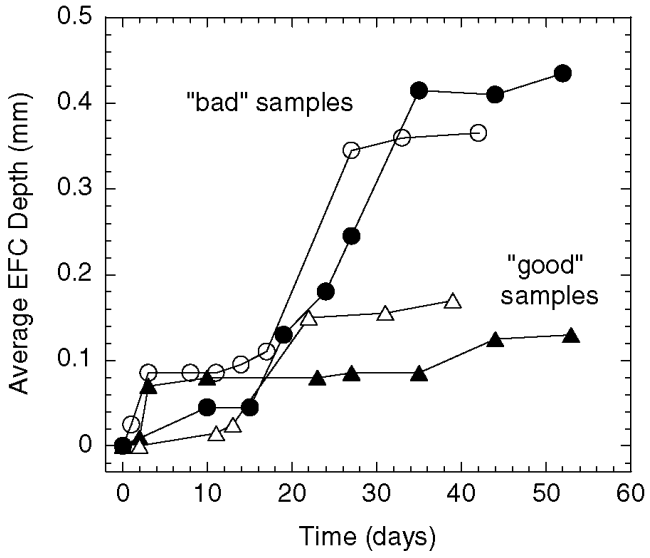

Fig. 5. Average exfoliation corrosion depth for duplicate samples of ‘‘good’’ (triangles) and ‘‘bad’’ (circles) AA7178 wingskin samples exposed to 96% RH.

ESH testing was performed on ‘‘good’’ and ‘‘bad’’ samples under a range of constant humidity, Fig. 6. The two plates exhibited different exfoliation behavior in different humidities. In the lowest humidity (30%, $CaCl_2$), the surfaces of both samples were still shiny after 60 days exposure, and no EFC was evident. This humidity is apparently below the critical humidity of the environment deposited in the localized corrosion sites during the electrochemical pretreatment. This environment dried completely, preventing further attack. In about 50% RH, some product exuded out of the surface and EFC was seen on the downside of the ‘‘good’’ sample after 3 days. However, the EFC ceased after that time, perhaps because it took some time for the environment in the pretreatment sites to equilibrate with the humidity in the chamber and dry out. Above around 50% RH, samples exfoliated more severely with increasing humidity. The average EFC rate was 3.0, 4.0, and 14.0 μm/day for the ‘‘bad’’ samples in 66%, 76%, and 96% RH, respectively. For ‘‘good’’ samples, the values were 0.6, 0.8, and 5.0 μm/day, respectively, for the same humidities. The effect of humidity and other factors on EFC rate will be covered in detail in a subsequent communication [24]. However, it is clear from these data that the rate of EFC increases with increasing humidity above a critical humidity.

3.2. Optical microscopy

The microstructures of the ‘‘good’’ and ‘‘bad’’ plates are given in Fig. 7, along with the convention utilized for the various sections. Fig. 8 is a montage of higher-magnification micrographs of the T sections of the two plates covering the full cross section from one side of the plate to the other. Each section is given in two parts, with some overlap of the top left and bottom right.

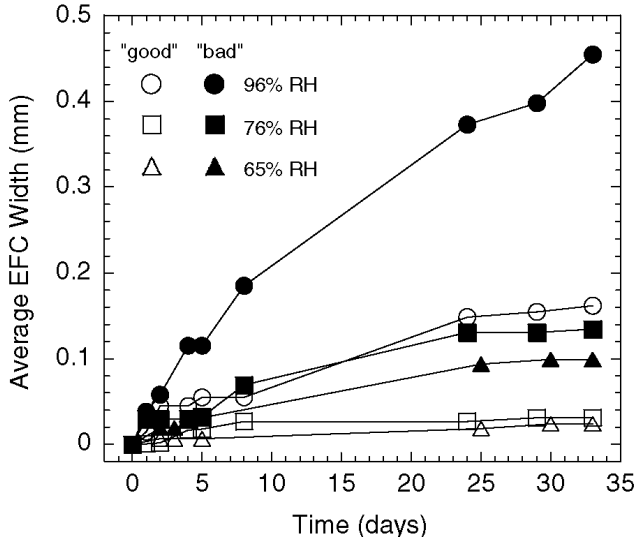

Fig. 6. Average exfoliation depths of ‘‘good’’ (open symbols) and ‘‘bad’’ (closed symbols’’ AA7178 wingskin samples exposed to different humidities: circles – 96%, squares – 76%, triangles – 65%).

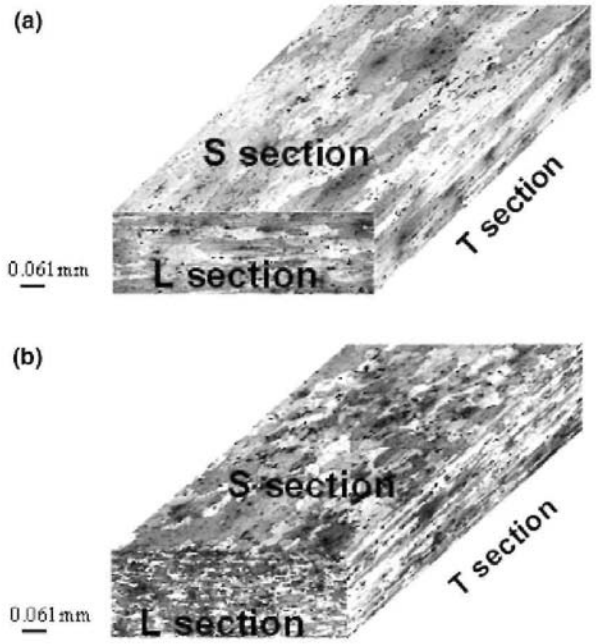

Fig. 7. Metallographic sections of ‘‘good’’ plate and ‘‘bad’’ plate. Also given is the terminology used for the different sections: (a) ‘‘bad’’ plate and (b) ‘‘good’’ plate.

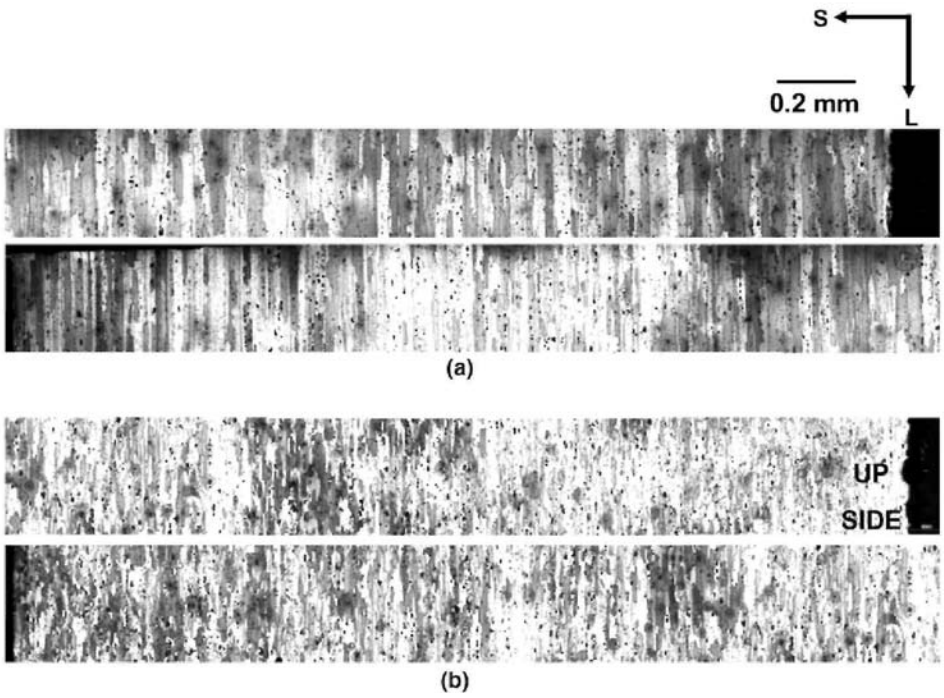

Fig. 8. Metallographic sections of AA7178 wingskin plate: (a) ‘‘bad’’ plate and (b) ‘‘good’’ plate. The sections are through-thickness montages, starting at the right of the top image in each pair and then wrapping around to end at the left side of the bottom image in each pair.

The grains in the ‘‘bad’’ plate are larger and more elongated in the L direction than in the ‘‘good’’ plate. In particular, the near-surface regions of the ‘‘good’’ plate exhibit much smaller grains with a smaller aspect ratio. The grain sizes of the ‘‘good’’ and ‘‘bad’’ plates as a function of the position through thickness direction were obtained by the analysis of L, T, and S cross-sections and are shown in Fig. 9. The grain aspect ratios in longitudinal and transverse orientations are reported in Fig. 9 with the L/S ratio shown above the T/S ratio. The ‘‘bad’’ plate has a higher grain aspect ratio than the ‘‘good’’ plate. In particular, the size of grains in the L direction is about 3 times greater in the ‘‘bad’’ plate. It is known that a microstructure with grains that are less-elongated should be more resistant to exfoliation (but should exhibit faster IGC in the S direction).

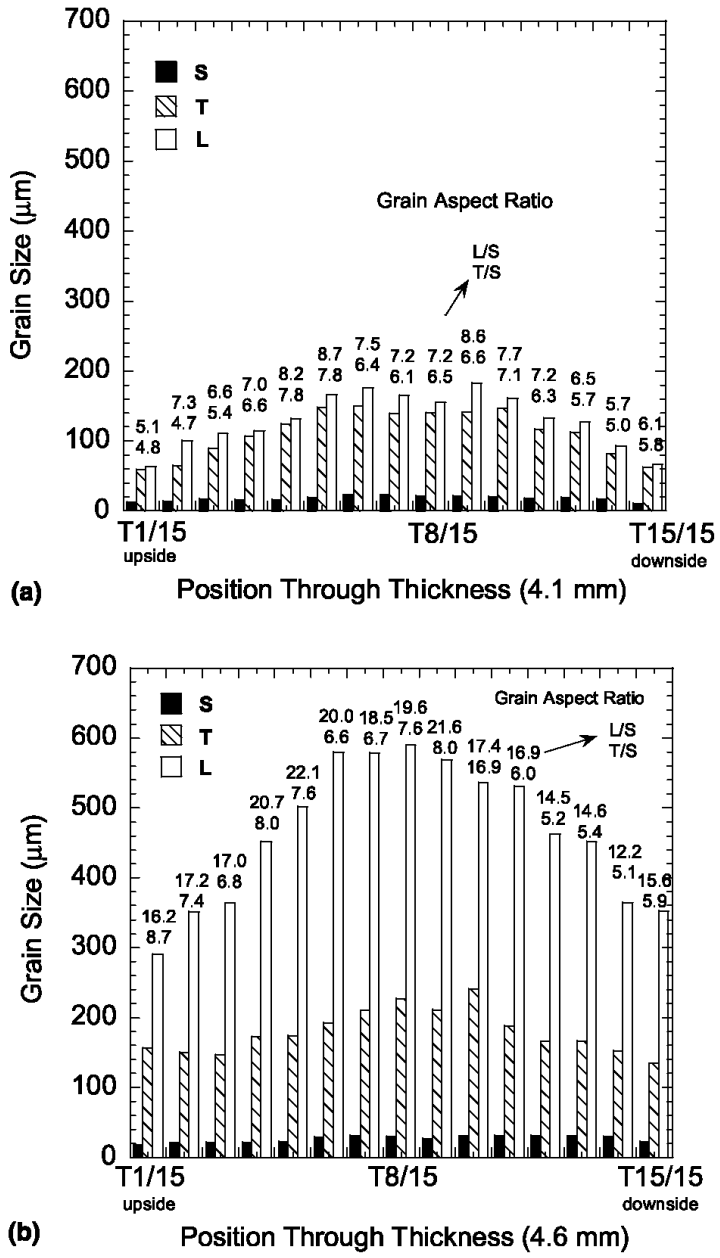

Fig. 9. Grain size distribution and grain aspect ratios through the thickness of (a) ‘‘good’’ plate and (b) ‘‘bad’’ plate.

The larger grain size and higher grain aspect ratio of the ‘‘bad’’ plate contribute to its higher EFC susceptibility. There is a small difference in the grain aspect ratio near the upside and downside of the ‘‘good’’ sample. However, it is unlikely that the slightly smaller grain aspect ratio at the upside is the sole explanation for the much better EFC resistance there. Furthermore, the grain size and grain aspect ratio near the downside of the ‘‘good’’ sample are much smaller than those of the ‘‘bad’’ sample, yet the EFC rate was similar. Therefore, factors other than grain size and shape must play a determining role in the EFC susceptibility. Possibilities include residual stress in the plate and local variations in grain boundary microchemistry.

3.3. TEM analysis

Analytical transmission electron microscopy (TEM) was used to investigate the composition of the grain boundary constituents in the ‘‘good’’ plate. Fig. 10 shows transmission electron micrographs of samples taken from near the up and downsides of the ‘‘good’’ plate. Both micrographs exhibit particles in the matrix as well as on the grain boundaries and a precipitate free zone (PFZ) on either side of the grain boundaries. The width of the PFZ near the upside of the ‘‘good’’ plate was around 90–100 nm, which is somewhat larger than the PFZ width near the downside, less than 50 nm. There was no clear difference in the size, distribution, and composition of the large precipitates in the matrix near the two surfaces. EDS line profiling was performed across grain boundaries at locations that include precipitates and locations away from precipitates to analyze the PFZ. Four different precipitates and five different PFZs along grain boundaries near upside and downside of the ‘‘good’’ plate were analyzed. Figs. 11 and 12 show representative precipitates and PFZs that exist near the upside and downside of the plate. The lines in the higher resolution images in these figures show the paths of the line profiles in one measurement. The concentration profiles in the form of concentration ratios for various elements relative to Al are shown in Fig. 13 for the line-scans across the grain boundary precipitates in Fig. 11, and in Fig. 14 for the line scans across the grain boundary precipitate free zones in Fig. 12. The concentration ratios were determined using the appropriate *k* factors and the X-ray intensity ratios. Two kinds of precipitates were found along grain boundaries near both the upside and downside of the plate. One was Al–Zn–Mg–Cu–Cr precipitate (concentration profiles across these precipitates are shown in Fig. 13 a near upside of the plate and in Fig. 13c near the downside of the plate) and the other was Cu–Al precipitate (concentration profiles across these precipitates are shown in Fig. 13b near upside of the plate and Fig. 13d near the downside of the plate). There are no obvious differences in the precipitates near the up- and downsides of the plate. Furthermore, it is unlikely that a difference in the composition of grain boundary precipitates can explain the difference in EFC behavior because the precipitates are isolated along the boundaries in this material, i.e. they do not form a continuous pathway on the grain boundaries.

The concentration profiles in the form of concentration ratios for the line-scans in Fig. 12 across PFZ regions are shown in Fig. 14. Zn is seen to be depleted in the PFZ near the grain boundary at the upside surface relative to the nearby lattice, Fig. 14a. In contrast, there is no apparent Zn depletion in the PFZ near the grain boundary at the down side surface, Fig. 14b. As noted above, only a limited number of different grain boundaries were analyzed (five near the upside and five near the downside). It is always possible to question the validity of using a limited number of very local TEM measurements to explain bulk properties. Nonetheless, the profiles shown in Fig. 14 are representative of the regions studied, and a difference in Zn concentration in the PFZ regions near the upside and downside was clearly evident.

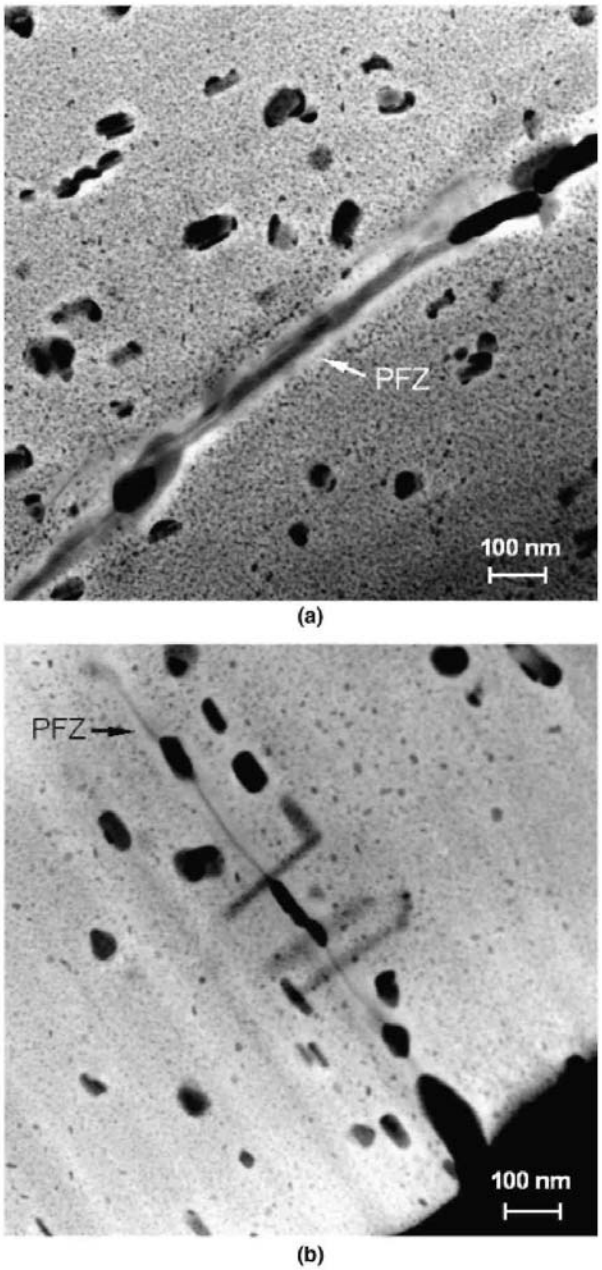

Fig. 10. TEM micrographs of grain-boundary in AA7178 ‘‘good’’ plate: (a) near up side of the ‘‘good’’ plate and (b) near down side of the ‘‘good’’ plate.

It is known that Zn, the main alloying element in 7xxx alloys, diffuses readily at normal homogenizing temperatures. This element has high diffusion rates and low solubility in Al, resulting in the formation of Mg–Zn containing phases along grain boundaries and the depletion of Mg and Zn in the area adjacent to the grain boundaries [5].

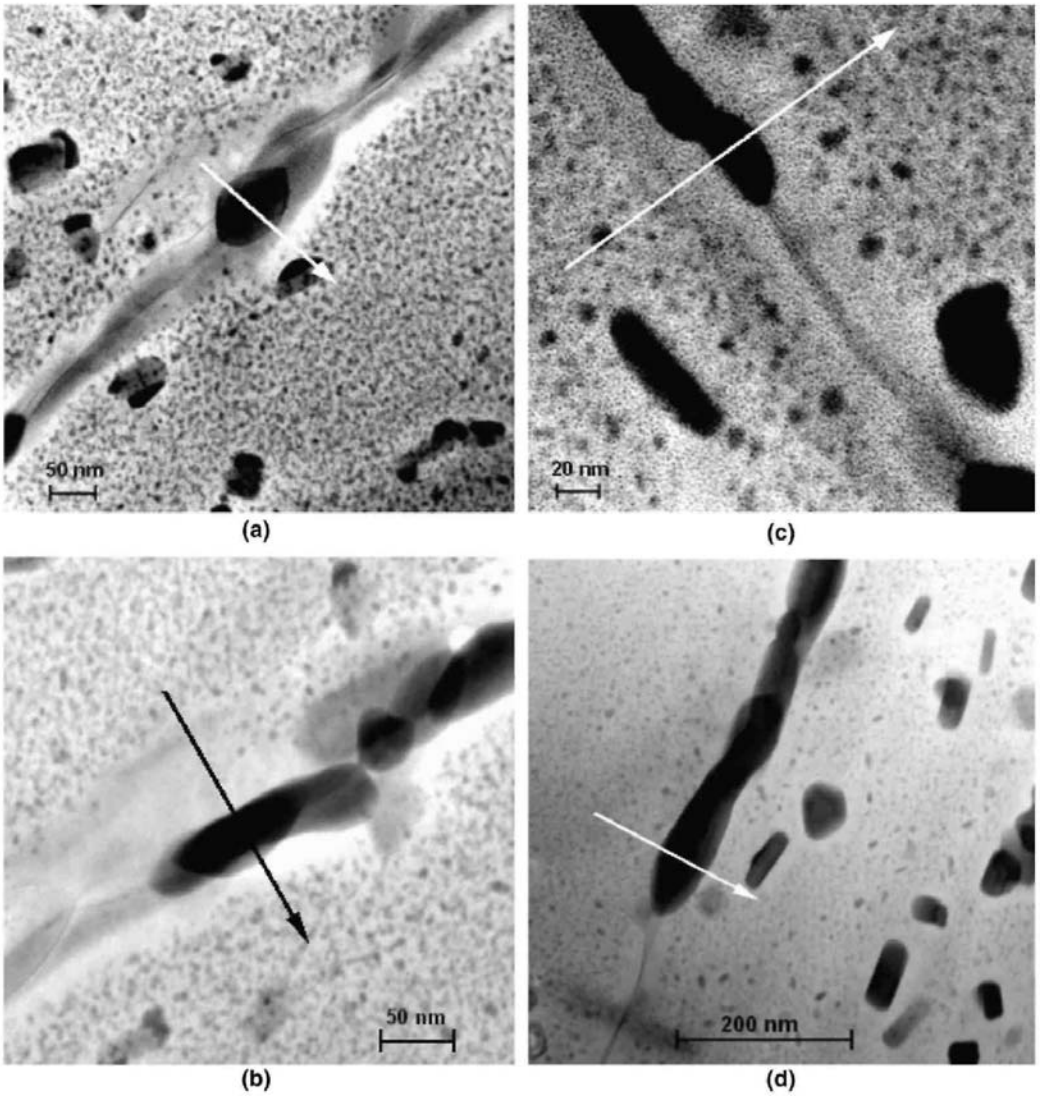

Fig. 11. TEM micrographs of grain-boundary in AA7178 showing Nano EDS line profiling across two different types of the GB precipitates (a,b) near up side of the ‘‘good’’ plate and (c,d) near down side of the ‘‘good’’ plate.

Park and Ardell used analytical transmission electron microscopy to show that the grain boundary region in AA7150-T6 exhibited considerable Zn depletion relative to the matrix [25]. Many studies have shown that the alloying of aluminum with Zn reduces the pitting potential and repassivation potentials [26–29]. Ramgopal et al. investigated the dissolution kinetics of binary Al alloys containing Cu, Zn and Mg in chloride solution and found that Zn addition decreased the repassivation potential by increasing the dissolution kinetics at a given potential [30].

The TEM results in this study suggest that the difference in Zn concentration in the PFZs near the upside and downside surfaces of the ‘‘good’’ plate is at least partly responsible for the difference in EFC behavior.

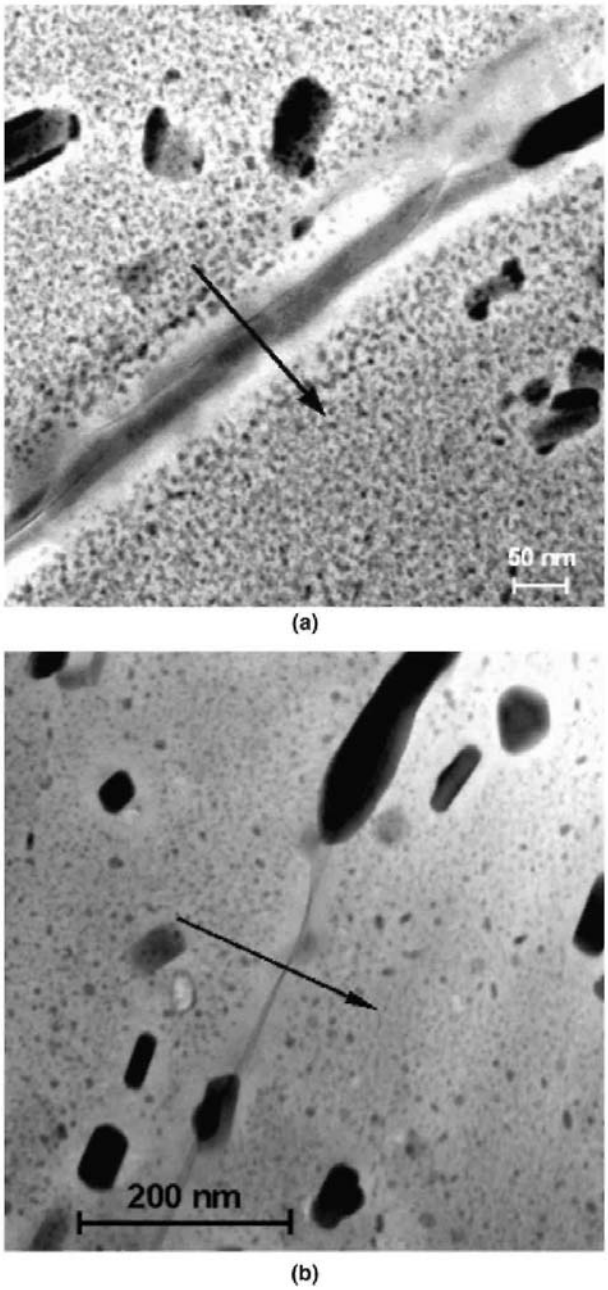

Fig. 12. TEM micrographs of grain-boundary in AA7178 showing Nano EDS line profiling across the GB PFZ: (a) near up side of the ‘‘good’’ plate and (b) near down side of the ‘‘good’’ plate.

This different distribution of Zn might be caused by details of the plate processing. The Cr and Cu enrichment in GB precipitates results in depletion of these two elements in grain boundary area. The PFZ is anodic to the rest of the grain and is preferentially attacked. In PFZs near the upside surface of this plate, the absence of solute Zn increased the corrosion resistance of the PFZ and reduced the susceptibility to IGC and thus EFC. On the other hand, the presence of Zn in the PFZ near the downside surface sharpened the electrochemical heterogeneity between the grain boundaries and the adjacent regions and hence enhanced EFC. The grain boundary

chemistry seems to be an important factor controlling the susceptibility to EFC.

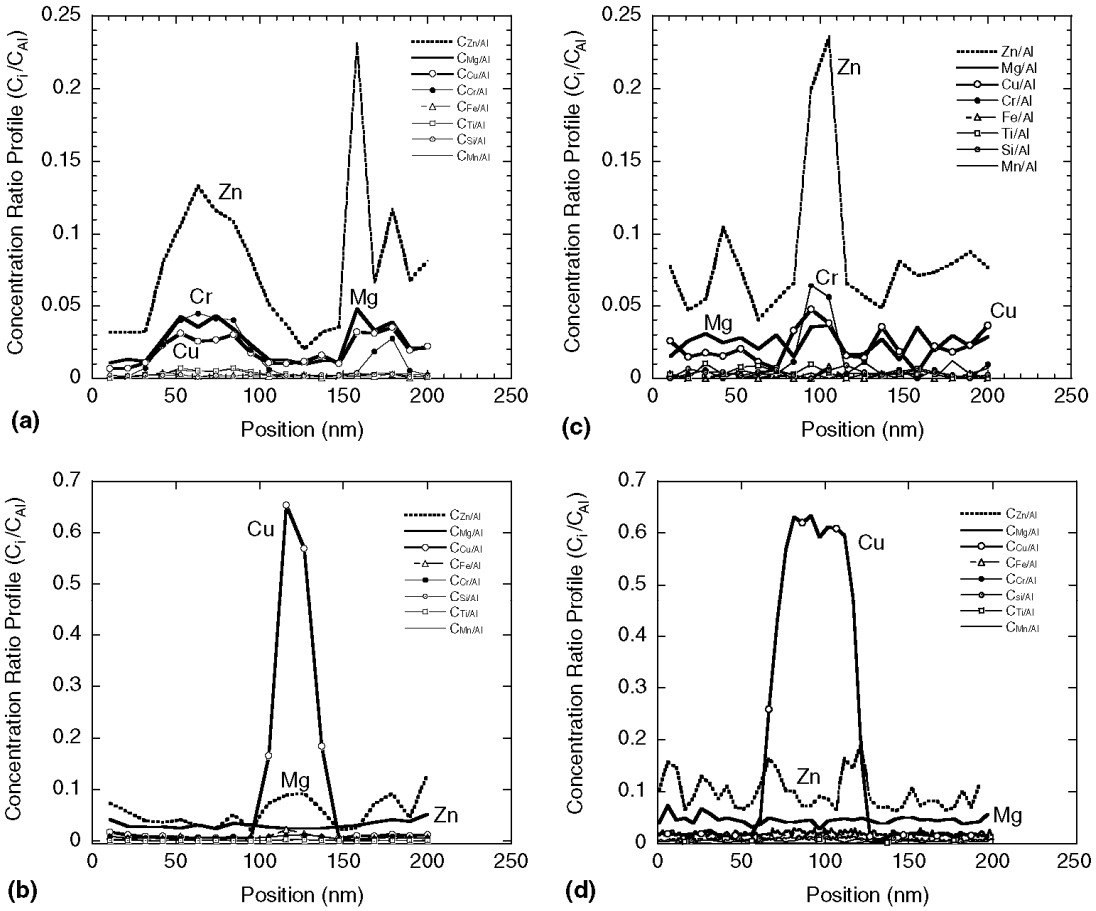

Fig. 13. Nano-EDS line profile of grain boundary precipitates. (a,b) linescans across grain boundary precipitates in Fig. 11a and b near upside of the ‘‘good’’ plate. (c,d) linescans across grain boundary precipitates in Fig. 11c and d near downside of the ‘‘good’’ plate. The data are reported as ratio of the X-ray intensities for each element relative to that of Al.

4. Conclusions

1. The exfoliation of slices in humidity (ESH) test was used to assess the susceptibility of AA7178 samples to exfoliation corrosion (EFC) and to determine the rate of EFC. In this test, samples sliced in a particular orientation are given an electrochemical pretreatment and then exposed in a constant humidity environment.
2. The ESH test was able to reproduce exfoliation behavior of plates observed during outdoor exposure. The high outdoor EFC rate for one plate resulted from the existence of susceptible regions in the plate and the chance location of such a region at the exposed surface.
3. EFC was not observed below 50% RH and the EFC kinetics increased with increasing humidity above this critical humidity.

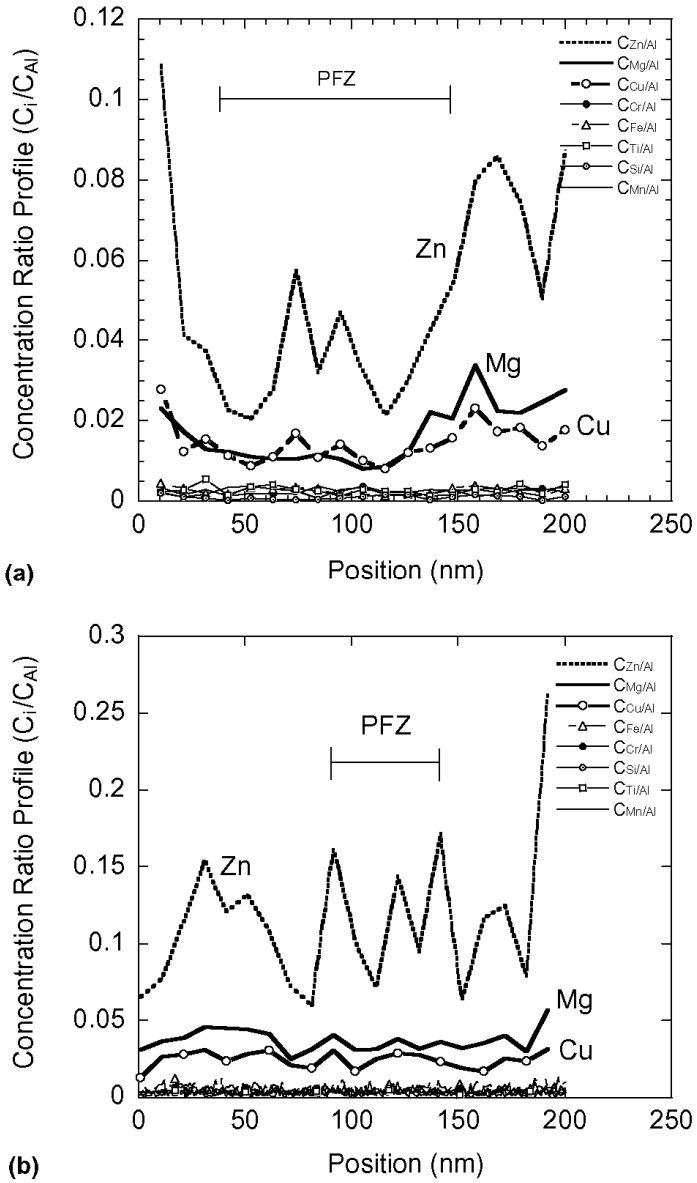

Fig. 14. Nano-EDS line profile of solute depleted zone around grain boundary. The data are reported as ratio of the X-ray intensities for each element relative to that of Al: (a) near up side of the ‘‘good’’ plate (shown in Fig. 12a) and (b) near down side of the ‘‘good’’ plate (shown in Fig. 12b).

4. EFC susceptibility was found to depend on grain size and shape as well as grain boundary composition.
5. A high susceptibility of regions in the AA7178 plate to EFC was associated with a high Zn content in the precipitate free zone at grain boundaries.

Acknowledgements

The authors acknowledge the support of the Aging Aircraft Division of ASC in support of the Aeronautical Enterprise Structures Strategy with a contract through S&K Technologies. The material was provided by W. Abbott

from Battelle, who also did the atmospheric exposure testing.

References

[1] Standard Test Method for Exfoliation Corrosion Susceptibility in 2xxx and 7xxx Series Aluminum Alloys (EXCO Test), The American Society for Testing and Materials, Philadelphia,PA, 1990.

[2] J.P. Chubb, T.A. Morad, B.S. Hockenhull, J.W. Bristow, The effect of exfoliation corrosion on the fracture and fatigue behavior of 7178-T6 aluminum, International Journal of Fatigue 17 (1995) 49–54.

[3] S. Lee, B.W. Lifka, in: V.S. Agarwala, G.M. Ugiansky (Eds.), Modification of the EXCO Test Method for Exfoliation Corrosion Susceptibility in 7XXX, 2XXX and Aluminum-Lithium Alloys, American Society for Testing and Materials, Philadelplia, 1992.

[4] B.W. Lifka, D.O. Sprowls, An improved exfoliation test for aluminum alloys, Corrosion 22 (1966) 7–15.

[5] D.G. Evans, P.W. Jeffrey. Exfoliation corrosion of AlZnMg alloys, in: R.W. Staehle, B.F. Brown, J. Kruger, A. Agarwal (Eds.), U.R. Evans Conference on Localized Corrosion, NACE-3, Houston, TX, 1974.

[6] G.S. Haynes, R. Baboian, Modified Salt Spray (Fog) Testing, Laboratory Corrosion Tests and Standards, ASTM, Philadelphia, PA, 1985.

[7] D.O. Sprowls, J.D. Walsh, M.B. Shumaker, Simplified exfoliation testing of aluminum alloys, Localized Corrosion-Cause of Metal Failure, ASTM STP 516, American Society for Testing and Materials, Philadelphia, PA, 1972.

[8] R. Braun, Exfoliation corrosion testing of aluminum alloys, British Corrosion Journal 30 (1995) 203–208.

[9] B.W. Lifka, D.O. Sprowls, Relationship of Accelerated Test Methods for Exfoliation Resistance in 7xxx Series Aluminum Alloys with Exposure to a Seacoast Atmosphere, ASTM Special Technical Publication 558, Philadelphia, PA, 1973.

[10] D.O. Sprowls, T.J. Summerson, F.E. Loftin, Exfoliation Corrosion Testing of 7075 and 7178 Aluminum Alloys-interim Report on Atmospheric Exposure Tests, ASTM Special Technical Publication 558, Philadelphia, PA, 1973.

[11] E.A.G. Liddiard, J.A. Whittaker, H.K. Farmery, The Exfoliation Corrosion of Aluminum Alloys, Journal of the Institute of Metals 89 (1960–1961) 377–384.

[12] M.J. Robinson, Mathematical modeling of exfoliation corrosion in high strength aluminum alloys, Corrosion Science 22 (1982) 775–790.

[13] M.J. Robinson, N.C. Jackson, The influence of grain structure and intergranular corrosion rate on exfoliation and stress corrosion cracking of high strength Al–Cu–Mg-alloys, Corrosion Science 41 (1999) 1013–1028.

[14] M.J. Robinson, N.C. Jackson, Exfoliation corrosion of high strength Al–Cu–Mg alloys: effect of grain structure, British Corrosion Journal 34 (1999) 45–49.

[15] T. Ramgopal, P.I. Gouma, G.S. Frankel, Role of grain-boundary precipitates and solute depleted zone on the intergranular corrosion, Corrosion 58 (2002) 687–697.

[16] S. Maitra, G.C. English, Mechanism of localized corrosion of 7075 alloy plate, Metallurgical Transactions A 12A (1981) 535–541.

[17] T. Ramgopal, P. Schmutz, G.S. Frankel, Electrochemical behavior of thin film analogs of Mg(Zn,Cu,Al), 2, Journal of The Electrochemical Society 148 (2001) B348–B356.

[18] E. Mattsson, L.O. Gullman, L. Knutsson, R. Sundberg, B. Thundal, Mechanism of exfoliation (layer corrosion) of Al–5%Zn–1%Mg, British Corrosion Journal 6 (1971) 73–83.

[19] G. Bassi, J.J. Theler, Effect of high temperature annealing on the microstructure of an AlZnMg alloy and the susceptibility to layer and stress corrosion of the corresponding sheet, Zeitschrift fur Metallkunde 60 (1969) 179–184.
[20] W. Abbott, personal communication.
[21] X. Zhao, Exfoliation Corrosion Kinetics of High Strength Aluminum Alloys, Ph.D. thesis, The Ohio State University, 2006.
[22] R.C. Weast (Ed.), Handbook of Chemistry and Physics, 61st ed., CRC Press, Boca Raton, FL, 1980.
[23] Q. Meng, G.S. Frankel, Effect of Cu content on corrosion behavior of 7xxx series aluminum alloys, Journal of The Electrochemical Society 151 (2004) B271–B283.
[24] X. Zhao, G.S. Frankel, Effects of RH, temper and stress on exfoliation corrosion kinetics of AA7178, Corrosion, submitted for publication.
[25] J.K. Park, A.J. Ardell, Microchemical analysis of precipitate free zones in 7075-Al in the T6, T7 and PRA tempers, Acta Metallurgica et Materialia 39 (1991) 591–598.
[26] I.L. Muller, J.R. Galvele, Pitting potential of high purity binary aluminum alloys II. Al–Mg and Al–Zn Alloys,, Corrosion Science 17 (1977) 995–1007.
[27] F. Sato, R.C. Newman, Mechanism of activation of aluminum by low melting point elements: Part 1 – effect of zinc on activation of aluminum in metastable pitting, Corrosion 54 (1998) 955.
[28] F. Sato, R.C. Newman, Mechanism of activation of aluminum by low-melting point elements: Part 2 – effect of zinc on activation of aluminum in pitting Corrosion, Corrosion 55 (1999) 3.
[29] P.L. Bonora, G.P. Ponzano, V. Lorenzelli, Localized corrosion of aluminum and its alloys. I. Critical potential, ER, with respect to pitting, British Corrosion Journal 9 (1974) 108–111.
[30] T. Ramgopal, G.S. Frankel, Role of alloying additions on the dissolution kinetics of aluminum binary alloys using artificial crevice electrodes, Corrosion 57 (2001) 702–711.